JOURNAL OF Materials CHEMISTRY

A computer modelling study of the effect of water on the surface structure and morphology of fluorapatite: introducing a $Ca_{10}(PO_4)_6F_2$ potential model

Donald Mkhonto[a] **and Nora H. de Leeuw***[b]

[a]*Materials Modeling Center, University of the North, Sovenga 0272, South Africa*
[b]*Department of Chemistry, University of Reading, Whiteknights, Reading, UK RG6 6AD. E-mail: n.h.deleeuw@reading.ac.uk*

Received 29th April 2002, Accepted 6th June 2002
First published as an Advance Article on the web 9th July 2002

We have derived a potential model for fluorapatite $Ca_{10}(PO_4)_6F_2$, fitted to structure, elastic constants and vibrational frequencies of the phosphate groups, which is compatible with existing calcite and fluorite potential models. We then modelled the structure and stabilities of the dry and hydrated {0001}, {10$\bar{1}$0}, {10$\bar{1}$1}, {11$\bar{2}$0}, {10$\bar{1}$3} and {11$\bar{2}$1} surfaces, which calculations confirmed the experimental dominance of the {0001} surface, which is prominently expressed in the calculated thermodynamic morphologies. The dehydrated morphology further shows the experimental {11$\bar{2}$1} twinning plane, while the {10$\bar{1}$0} cleavage plane is expressed in the hydrated morphology. Molecular adsorption of water has a stabilising effect on all six surfaces, where the surfaces generally show Langmuir behaviour and the calculated hydration energies indicate physisorption (73–88 kJ mol^{-1}). The chains of fluoride ions surrounded by hexagonal calcium channels can become distorted in two major ways: either by a shortening/lengthening of the F–F distances, when the channel is perpendicular to the surface, or by distortion of the Ca–F bonds when the channel is parallel to the surface. Both distortions occur when the channel runs at an angle to the surface. Other relaxations include compression of the calcium sub-lattice and rotation of surface phosphate groups.

Introduction

Apatite minerals are the most abundant phosphorus-bearing materials and are found in almost all igneous rocks and to a lesser extent in sedimentary and metamorphic rocks. The isomorphous series can be represented by fluorapatite $Ca_{10}(PO_4)_6F_2$, which is by far the most common, chlorapatite $Ca_{10}(PO_4)_6Cl_2$, hydroxyapatite $Ca_{10}(PO_4)_6(OH)_2$ and carbonate-apatite $Ca_{10}(PO_4,CO_3,OH)_6(F,OH)_2$.[1] Although complete solid solutions of the monovalent anions (OH^-,F^-,Cl^-) are obtained in synthetic apatites, it is not clear whether this is also the case in natural apatites.[2] However, the distribution of the different types of anions through the lattice influences some physical properties such as melting, dissolution and diffusion behaviour and hence, insight in the microscopic structure of the apatite mixtures and the bulk distribution of the anions, whether uniform or in domains, will help the understanding of these macroscopic properties.

In geological situations, apatites are often used as geo- and thermo-chronometers, either by measuring fission tracks of thorium and uranium,[3–5] argon dating[6] or the retention of ^4He, the decay product of uranium and thorium.[7,8] In addition, the presence and isotopic composition of noble gases in apatites can give an insight into mantle processes in the past. It is therefore necessary to understand the diffusion behaviour of species such as helium, xenon and argon through the apatite if our interpretation of the data relating to these processes is to be reliable.[9,10] Although the most common naturally occurring apatite is fluorapatite, the presence of Cl^- ions substituting for the F^- ions is thought to affect He diffusion. Furthermore, because of their affinity for impurity ions, apatites may well become important as environmental sinks for the uptake of heavy metals and radio-active contaminants, such as lead and uranium.

Hydroxyapatite is the major constituent of mammalian bones and tooth enamel, and because of this importance as a natural bone material, apatite is a possible candidate in the manufacture of artificial bones. In addition, fluoridation of hydroxyapatite can suppress dental decay, for example, by the production of fluorapatite, which is less soluble than hydroxyapatite. As apatites are thus important materials in both geological and biological situations, and because of their natural abundance as common accessory minerals in many types of rock, it is of basic interest to gain a detailed understanding of the crystal formation,[11] dissolution processes[12] and interfacial interactions between the crystalline and amorphous phases. The surface structure and reactivity of the apatite material is of direct relevance for these processes and hence, in this work we have employed classical atomistic simulation methods to model the structure and stability of both dehydrated and hydrated fluorapatite surfaces and the effect of surface hydration on the crystal morphology.

Computational methods

The structures and energies of the fluorapatite surfaces were modelled using classical energy minimisation techniques. These atomistic simulation methods are based on the Born model of solids,[13] which assumes that the ions in the crystal interact *via* long-range electrostatic forces and short-range forces, including both the repulsions and the van der Waals attractions between neighbouring electron charge clouds, which are described by simple analytical functions. The electronic polarisability of the ions is included *via* the shell model of Dick and Overhauser[14] in which each polarisable ion, in our case the oxygen and fluoride ions, is represented by a core and a massless shell, connected by a spring. The polarisability of the model ion is then determined by the spring constant and the charges of the core and shell. When necessary, angle-dependent forces are included to allow directionality of bonding as, for example, in the covalent phosphate anion.

Although the potential model for fluorapatite used in this work was fitted to bulk properties, it is generally possible for ionic materials to transfer potential parameters to surface calculations. In semiconductors, where the surface involves breaking bonds, and in metals where the surface means a sudden change in the electron density, there is often a problem with transferability from bulk potential parameters to surfaces. However, in ionic materials after relaxation, the Madelung potentials are 90% or more of the bulk values and hence the change of ionic radii is negligible. For example, the $CaCO_3$ potential parameters, which were used in the derivation of the fluorapatite potential model in this work, were derived by Pavese *et al*. for bulk calcite,[15] but they have subsequently been shown to accurately reproduce experimental surface features and processes, see, for example, refs. 16–19. Since the surfaces considered in this work leave the phosphate group intact (like the carbonate group in calcium carbonates), the bulk derived potential model will be adequate.

The energy minimisation codes employed for the derivation of the potential model and the calculation of the bulk crystal properties were PARAPOCS[20] and GULP,[21] while the surfaces were modelled using the code METADISE,[22] which is designed to model dislocations, interfaces and surfaces. Tasker[23] identified three different types of surfaces, (i) an uncharged plane with cations and anions in stoichiometric ratio, (ii) a stack of charged planes where the repeat unit perpendicular to the surface has no dipole moment, and finally (iii) a stack of charged planes where the repeat unit has a dipole moment perpendicular to the surface. In the last instance the surface needs to be reconstructed to remove the dipole. This is often achieved by creating surface vacancies. Following the approach of Tasker,[23] the crystal consists of a series of charged planes parallel to the surface and periodic in two dimensions. The crystal is divided into two blocks each comprising two regions, region I and region II. Region I contains those atoms near the surface, which are allowed to relax to their mechanical equilibrium, while region II contains those atoms further away, which represent the rest of the crystal and are kept fixed at their bulk equilibrium position. Inclusion of region II is necessary to ensure that the potential of an ion at the bottom of region I is modelled correctly. The bulk of the crystal is simulated by the two blocks together while the surface is represented by a single block with the top of region I as the free surface. Interfaces such as stacking faults and grain boundaries can be studied by fitting two surface blocks together in different orientations. Both regions I and II need to be sufficiently large for the energy to converge. The energies of the blocks are essentially the sum of the energies of interaction between all atoms.

The surface energy γ is a measure of the thermodynamic stability of the surface with a low, positive value indicating a stable surface. It is given by:

$$\gamma = \frac{U_S - U_B}{A}$$

where U_S is the energy of the surface block of the crystal, U_B is the energy of an equal number of atoms of the bulk crystal and A is the surface area. The surface energy is thus the energy required to cleave the crystal, exposing the surface. The energies of the blocks are essentially the sum of the energies of interaction between all atoms. The long-range Coulombic interactions are calculated using the Parry technique[24,25] whereas the short-range repulsions and Van der Waals attraction are described by parameterised analytical expressions.

For the hydrated surfaces the surface energies were calculated with respect to liquid water in order to assess the stability of the surface in an aqueous environment:

$$\gamma_H = \frac{U_H - (U_B + U_{H_2O(l)})}{A}$$

where U_H is the energy of the surface block, suitably hydrated, while $U_{H_2O(l)}$ is the energy of bulk water. The latter is the sum of the self-energy of water due to the intra-molecular forces, and the energy of condensation due to the intermolecular forces. For associative adsorption we calculated the self-energy to be -878.0 kJ mol^{-1} and we obtained an energy of condensation of -43.0 kJ mol^{-1} from molecular dynamics (MD) simulations,[26] which agrees well with the experimental value of -43.4 kJ mol^{-1}.[27] Thus the new surface energy is simply equivalent to the sum of the energy required to cleave the crystal and then add water to the surface.

In addition to calculating the surface energy we calculated the adsorption energy U_{ads}, *i.e*. the energy to adsorb water on the surface per water molecule, which is given by:

$$U_{ads} = \frac{U_H - (U_S + nU_{H_2O(g)})}{n}$$

where n is the number of water molecules and $U_{H_2O(g)}$ is the energy of a gaseous water molecule. Calculating the adsorption energy with respect to gaseous water means that we can compare our results directly with experimental techniques such as temperature programmed desorption (TPD). We need of course to be confident that in each case the most stable configuration of the surface with adsorbed water is found, locating as far as possible the global rather than a local minimum. Thus, many possible configurations were investigated, varying both adsorption sites, coverage and initial position of the water molecules. All energies quoted are those of the most stable relaxed surface configurations found.

Potential model

The reliability of the calculated surface and adsorption energies depends on the accuracy of the potential model. Table 1 lists the potential parameters derived and employed in this work. Although other potential models for fluorapatite are available, *i.e*. those of Lee *et al*.[28] and Meis *et al*.,[29] apatite co-exists with both calcite ($CaCO_3$) and fluorite (CaF_2) in mineral deposits and hence we sought to derive a potential model for fluorapatite that was compatible with existing models for calcite and fluorite, so that in future we may model interfaces and substitutional defects between these three minerals. The Ca–O and Ca–F parameters in the fluorapatite potential were therefore taken from the calcium carbonate and calcium fluoride potentials developed by Pavese *et al*.[15] and Catlow *et al*.[30] respectively, where the oxygen and fluorine core–shell charges and interactions were also kept at the values derived by Pavese *et al*.[15] and Catlow *et al*.[30] for calcite and fluorite. All other potential parameters, such as the interactions between oxygen and fluoride ions and between oxygen and phosphorus within the phosphate groups, were fitted empirically to a variety of experimental parameters, such as the crystal structure and elastic constants, bond dissociation energies and vibrational data of the phosphate group. All short-range interactions involving anions are between the shells apart from the Morse potential in the phosphate group, which acts between the phosphorus and oxygen cores.

The O–F short-range interactions were fitted to the fluorapatite structure and elastic constants and optimised using the GULP program.[21] They are described by an effective Buckingham potential:

$$\Phi_{ij}(r_{ij}) = A_{ij} e^{-\frac{r_{ij}}{\rho_{ij}}} - \frac{C_{ij}}{r_{ij}^6}$$

where r_{ij} is the separation and where classically the parameters A_{ij} and ρ_{ij} are the size and hardness of the ion, respectively.

Table 1 Potential parameters used in this work (short-range cutoff 20 Å)

Ion	Charge (e)		Core–shell interaction /eV Å^{-2}
	Core	Shell	
Ca	+2.000		
P	+1.180		
F	+1.380	−2.380	101.2000
Phosphate oxygen (O)	+0.587	−1.632	507.4000
Water oxygen (O_w)	+1.250	−2.050	209.4496

Buckingham potential			
Ion pair	A/eV	ρ/Å	C/eV Å^6
Ca–O	1550.0	0.29700	0.0
Ca–O_w	1186.6	0.29700	0.0
Ca–F	1272.8	0.29970	0.0
O–O	16372.0	0.21300	3.47
O–O_w	12533.6	0.21300	12.09
O–F	583833.7	0.21163	7.68
F–F	99731834.0	0.12013	17.02423
F–O_w	79785221	0.12013	26.78752
H–O	396.3	0.23000	0.0
H–O_w	396.3	0.25000	10.0
H–F	715.34	0.25000	10.0

Lennard-Jones potential		
Ion pair	A/eV Å^{12}	B/eV Å^6
O_w–O_w	39344.98	42.15

Morse potential			
Ion pair	D/eV	α/Å^{-1}	r_0/Å
P_{core}–O_{core}	3.47	2.030	1.600
H–O_w	6.203713	2.22003	0.92376

Three-body potential		
	k/eV rad^{-2}	Θ_0
O_{core}–P–O_{core}	1.322626	109.470000
H–O_w–H	4.199780	108.693195

Intramolecular Coulombic interaction (%)	
H–O_w	50
H–H	50

However, in an effective pair potential as used here the A_{ij} and ρ_{ij} terms have become more or less fused, *i.e.* they are interdependent and hence their physical meaning is less certain. The first term then represents the short-range repulsive interaction between the ions while the second term represents the attractive van der Waals forces.

The bonding between the phosphorus and oxygen ions within the phosphate group is partially covalent, as was shown by electronic structure calculations of fluorapatite,[31] which we describe by a Morse potential:

$$\Phi_{ij}(r_{ij}) = D(1 - e^{[-\alpha(r_{ij} - r_0)]})^2 - D$$

where D is the dissociation energy of the bond, r_0 is the equilibrium separation and α is a variable which can be determined by spectroscopic data. The value of D was taken as the experimental bond dissociation energy of a single P–O bond, which is 335 kJmol^{-1}.[32] The four P–O bondlengths in the experimental fluorapatite structure are not equal (1.5–1.8 Å) but as the Morse potential is capable of modelling anharmonicity, interionic distances away from the equilibrium bond distance can also be simulated. r_0 was therefore set at 1.6 and α was then fitted to the four phosphate stretching modes, which were obtained for apatite by Taylor *et al.*[33] using Raman and inelastic neutron scattering techniques. We fitted the α parameter to the mean value of the four Raman active vibrational frequencies as potential models often underestimate the coupling between modes and fitting to the four individual modes would therefore be meaningless.

Finally, a bond-bending term was introduced to allow directionality of bonding between the phosphorus and oxygen ions in the phosphate group:

$$\Phi_{ijk}(r_{ijk}) = \frac{1}{2} k_{ijk}(\theta_{ijk} - \theta_0)^2$$

which is a simple harmonic potential about the equilibrium bond angle, where k_{ijk} is the force constant and $(\theta_{ijk} - \theta_0)$ is the deviation of the bond from the equilibrium angle, which is set at the ideal tetrahedral angle of 109.47 °. This reflects the fact that the phosphorus is covalently bonded in a distorted tetrahedral geometry to three oxygen atoms at a distance of approximately 1.5–1.6 Å and a fourth at approximately 1.8 Å. The elastic constants were found to be fairly sensitive to the

force constant and hence allowed us a mechanism for the derivation of k_{ijk}, which was fitted to reproduce the experimental elastic constants.

The potential parameters used for the intra- and intermolecular water interactions are those described in a previous study of MD simulations on MgO surfaces, where the intramolecular interactions between oxygen and hydrogen atoms are described by a Morse potential and intermolecularly by a Buckingham potential. The steric effect that the electron lone pairs on the oxygen atom have on the geometry of the water molecule was included by partially removing the electrostatic interactions between the two hydrogen atoms and between hydrogen and oxygen atoms in the water molecule (by half), making the hydrogen atoms less repulsive, much as electrostatic interactions within organic molecules are routinely removed in potential models for biological applications.[26] For the interactions between water molecules and fluorapatite surfaces (the Ca–water and O–water interactions) we used the potential parameters previously fitted to calcite,[16] which were successfully used in simulations of water adsorption at calcium carbonate surfaces and the calculation of crystal morphologies and dissolution from calcite steps.[17,34,35] In addition, these potential parameters reproduce the experimental heat of formation of calcium carbonate from its aqueous ions to an acceptable degree of accuracy (within 20 kJ mol^{-1}), even though the parameters were not fitted to this process. The Ca–F parameters were validated by *ab initio* calculations.

Results and discussion

Fluorapatite has a hexagonal crystal structure with spacegroup $P6_3/m$.[1,2] The apatite structure is shown in Fig. 1, where the F^- ions in the structure are located one above the other in a column parallel to the *c*-axis (into the plane of the paper in Fig. 1). The fluoride ions in the hexagonal channels are surrounded by the calcium ions, whereby each F^- is coordinated to three calcium ions in the same *a*-*b* plane. We used the structure determined by Hendricks *et al.*[36] with $a = b = 9.370$ Å, $c = 6.880$ Å, where $\alpha = \beta = 90\,^\circ$, $\gamma = 120\,^\circ$. Upon energy minimisation of the bulk crystal, using the potential model derived above and listed in Table 1, the lattice parameters were calculated at $a = b = 9.375$ Å, $c = 6.871$ Å, $\alpha = \beta = 90\,^\circ$, $\gamma = 120\,^\circ$. Table 2 lists the calculated and experimental crystallographic coordinates of the constituent atoms, from which we see that the calculated structure is in good agreement with the experimental crystal structure, especially noting that there are no symmetry constraints in the calculations, *i.e.* once the simulation cell has been created from the spacegroup, all species in the simulation cell are free to move relative to each other and the cell itself is allowed to both expand or contract and to deform. A comparison of calculated and experimental physical properties of the material is made in Table 3, from which it is clear that the elastic constants are accurately reproduced, which is as expected as they were used for fitting the potential model. The P–O Morse potential was fitted to the mean value of the vibrational stretching frequencies of the phosphate group and the agreement between calculated and experimental values of the individual stretch frequencies are therefore not as good as the other properties to which the potential model was fitted. Experimentally, there is no agreement on values for the relative permittivities of apatite. Our calculated values of 7.1 and 4.5 do not agree very well with the experimental measurements of 10.4 and 8.3 by Shannon and Rossman.[37] However, these experimental values, which were obtained from a very substituted material containing many impurity ions, differ considerably from the generally accepted value of 7.4 for the relative permittivity of apatite,[38] which is also in line with those of similar materials such as 6.2 for forsterite (Mg_2SiO_4), 6.1–6.9 for calcium carbonate ($CaCO_3$) and 7.4 for fluorite (CaF_2). In addition, more recently the relative permittivity of apatite thin films was measured at 5.7.[39] We would therefore consider that the agreement between the calculated and experimental static relative permittivities is adequate, especially given the fact that the potential parameters were not fitted against these properties.

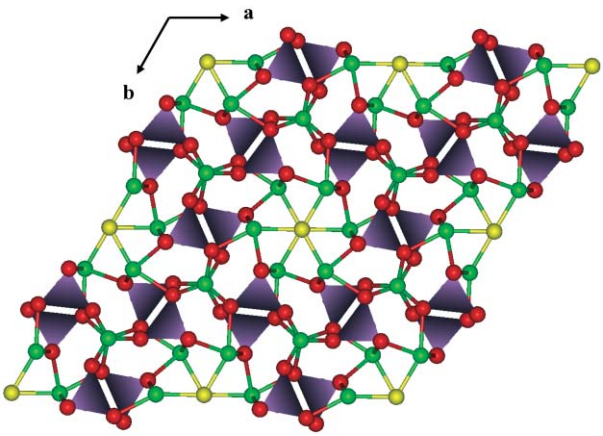

Fig. 1 Hexagonal structure of fluorapatite, viewed down onto the (0001) plane (Ca = green, O = red, P = purple, F = yellow, PO_4 groups displayed as tetrahedra).

Table 2 Calculated and experimental crystallographic data for $Ca_{10}(PO_4)_6F_2$

	Space group					
	$P6_3/m$			$P6_3/m$		
	Calculated[a]			Experimental [ref. 36]		
a,*b*,*c*	9.3750	9.3750	6.8712	9.3700	9.3700	6.8800
α,β,γ	90	90	120	90	90	120
Ca	0.3333	0.6667	−0.0004	0.3333	0.6667	0.0000
Ca	0.2504	−0.0050	0.2500	0.2500	0.0000	0.2500
P	0.4071	0.3744	0.2500	0.4170	0.3610	0.2500
O	0.3311	0.4874	0.2500	0.3333	0.5000	0.2500
O	0.5967	0.4693	0.2500	0.6000	0.4670	0.2500
O	0.3556	0.2652	0.0656	0.3333	0.2500	0.0630
F	0.0000	0.0000	0.2500	0.0000	0.0000	0.2500

[a]No symmetry constraints in the calculation.

Table 3 Calculated and experimental physical properties of $Ca_{10}(PO_4)_6F_2$

Property	Calculated	Experimental
Elastic constants/10^{10} Pa		
C_{11}	150.6	152.0[a]
C_{33}	176.6	185.7[a]
C_{44}	53.2	42.8[a]
C_{12}	62.8	50.0[a]
C_{13}	73.6	63.1[a]
Bulk modulus/GPa	98.8	93.4[b]
Static relative permittivity		
11	7.1	10.4[c]
33	4.5	8.3[c]
Phosphate mode/cm^{-1}		
ν_1	802	963[d]
ν_2	428	435[d]
ν_3	1072	1046[d]
ν_4	724	590[d]

[a]Ref. 55. [b]Ref. 56. [c]Ref. 37. [d]Ref. 33.

Surface simulations

We next created a range of surfaces with low Miller indices as these surfaces have the smallest inter-planar spacings and as a result are often the most stable. The surfaces studied were the

Table 4 Surface energies of bulk-terminated and geometry optimised dehydrated fluorapatite surfaces

Surface	$\gamma_{unrelaxed}$/J m^{-2}	$\gamma_{relaxed}$/J m^{-2}
(0001)	1.19	0.77
(10$\bar{1}$0)	2.84	1.32
(10$\bar{1}$1)	1.81	1.00
(11$\bar{2}$0)	2.28	1.12
(10$\bar{1}$3)	2.98	1.94
(11$\bar{2}$1)	2.62	1.11

{0001}, {10$\bar{1}$0}, {10$\bar{1}$1}, {11$\bar{2}$0}, {10$\bar{1}$3} and {11$\bar{2}$1} planes and their symmetry-related surfaces. The {0001} and to a lesser extent {10$\bar{1}$0} surfaces are experimental cleavage planes, while the {11$\bar{2}$1} and {10$\bar{1}$3} planes occur as twinning planes in the natural crystals. Previous electronic structure calculations of fluorapatite have shown that the phosphate groups themselves have considerable covalent character but as a group act as a polyanion[31,40] and we therefore kept the phosphate groups intact when creating the surfaces. We first calculated the surface energies of both the bulk-terminated and geometry optimised dry surfaces (Table 4), from which we see that the {0001} surface is by far the most stable surface with the lowest surface energy, both before and after relaxation. This stability is rather remarkable as this surface is a dipolar type III surface and hence contains surface calcium vacancies, which were introduced to remove the dipole. The low surface energy of the {0001} surface, however, agrees very well with the fact that the (0001) surface is the major cleavage plane of apatite.[1] A side view of the unrelaxed, bulk-terminated surface is shown in Fig. 2(a), where we see the calcium vacancy at the surface and the column of fluoride ions perpendicular to the surface. The distance between the surface calcium and the three oxygen ions below is 2.41 Å, while the bond length between the surface oxygen atom and its phosphorus atom is 1.54 Å. The fluoride ions are in the plane of the phosphorus and calcium ions and the distance between them down the column is 3.43 Å, which is indicated in Fig. 2(a), with a Ca–F bond length of 2.37 Å. Upon geometry optimisation of the surface (shown in Fig. 2b), we observe considerable relaxation of the first and to a lesser extent second and third surface layers, especially of the calcium and fluoride sub-lattices. The phosphate groups remain intact, with just a little rotation of the oxygen in the topmost surface layer towards the surface calcium ion, although the O–P bond length remains virtually the same at 1.55 Å. The Ca–O bond lengths to the three oxygen ions below also remain the same at 2.40 Å, but the calcium ion has also relaxed into the surface to form three additional bonds to the rotated surface oxygen ions at a short bond length of 2.36 Å. The column of fluoride ions has become distorted with the topmost ion relaxing out of the surface, while the second ion moves more into the bulk. The resulting F–F distance at 3.86 Å is considerably longer than in the bulk material (3.43 Å). In addition, the second to third F–F distance has shortened to 3.20 Å, while the third to fourth F–F distance has again lengthened with respect to the bulk distance to 3.50 Å. Hence, this rumpling of the fluoride sublattice is much more extensive effect ($\sim$12 Å into the bulk) than the surface relaxation of the calcium, which only significantly affects the topmost calcium ions. Despite the distortion of the fluoride chain, the Ca–F bond lengths at 2.36–2.38 Å remain virtually at their bulk value.

In the {10$\bar{1}$0} surface, the F^- columns lie in the plane of the surface, rather than perpendicular to the surface as in the case of the {0001} surface above. The surface can be terminated in four different ways, but the surface terminated by a plane of calcium and phosphate ions, where the fluoride channels are kept intact, is the most stable (Fig. 3). Even so, we can see from Table 4 that this surface is much less stable than the {0001} surface, although the surface energy decreases considerably upon geometry optimisation of the bulk-terminated surface to the fully relaxed plane. This stabilisation is again due to relaxation of the surface calcium ions into the surface, hence forming new bonds with surface oxygen ions which have become accessible due to rotation of the surface phosphate groups (Fig. 3). The fluoride channel is again distorted, but unlike the {0001} surface above, this time the F–F distances remain at their bulk value of 3.43 Å. The distortion now occurs between the fluoride ions and surrounding calcium ions, whereby alternate fluoride ions relax into the bulk, with shortening of the Ca–F bonds below the fluoride and lengthening of the one above, and up towards the surface, with lengthening of the Ca–F bond below the fluoride ion. The chain of fluoride ions is also slightly rumpled parallel to the surface, alternating towards the sides of the channel, with shortening or lengthening of the relevant Ca–F bond lengths in the plane of the surface. The different Ca–F bond lengths are shown in Fig. 3.

The {10$\bar{1}$1} surface has the lowest surface energy of the dry surfaces after the {0001} surface. It has the fluoride columns running diagonally through the crystal with respect to the surface, where the most stable termination is the one shown in Fig. 4, with each surface fluoride ion coordinated to two

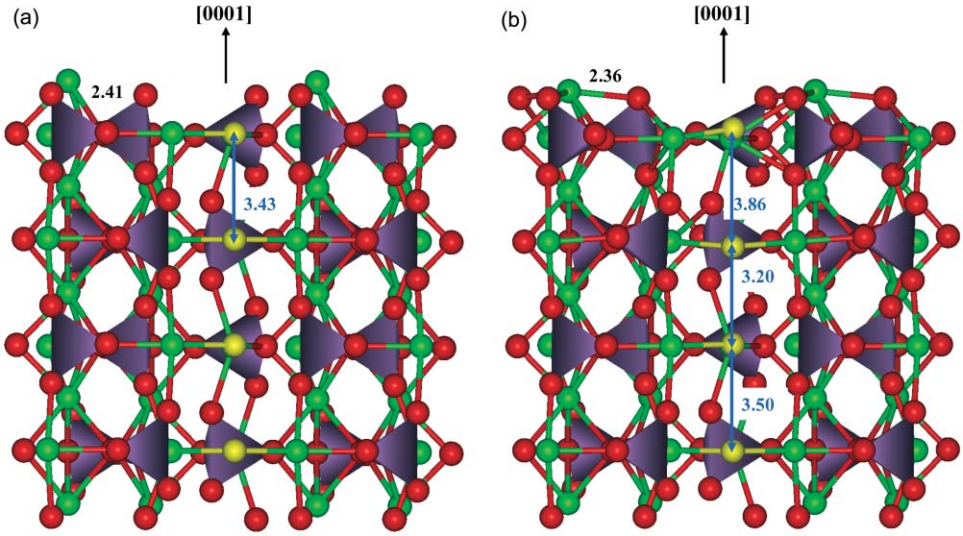

Fig. 2 Side view of (a) the bulk-terminated and (b) the geometry optimised {0001} surface, showing alternating lengthening and shortening of the F–F distances into the bulk material (Ca = green, O = red, P = purple, F = yellow, PO_4 groups displayed as tetrahedra).

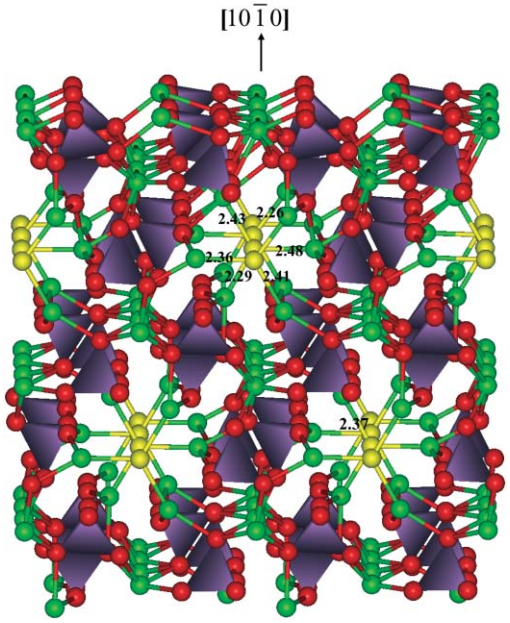

Fig. 3 Sideview of the geometry optimised {10$\bar{1}$0} surface, showing distortion of the Ca–F bonds in the hexagonal channels (Ca = green, O = red, P = purple, F = yellow, PO_4 groups displayed as tetrahedra).

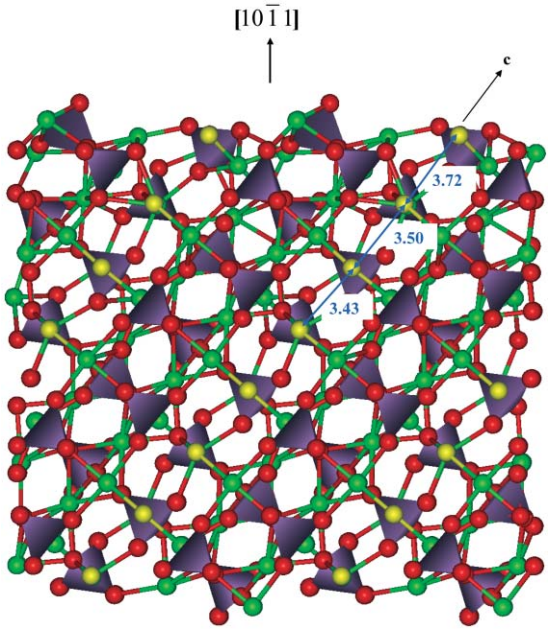

Fig. 4 Side view of the geometry optimised {10$\bar{1}$1} surface, showing lengthening of the F–F distances in the surface region (Ca = green, O = red, P = purple, F = yellow, PO_4 groups displayed as tetrahedra).

calcium ions below it. Again, there is distortion of the fluoride sublattice in the channel, with the distance from the surface F^- ions to the next ions in the channel expanding from the bulk value of 3.43 Å to 3.72 Å. However, this time the next F–F distance is not contracted as in the {0001} surface, but is also expanded to 3.50 Å. Thus, the distortion is an expansion of the fluoride chain in the surface region, rather than alternate lengthening and shortening of the interionic distances as was the case in the {0001} surface. The Ca–F distances in the surface region are also distorted. One of the Ca–F bonds to the surface fluoride ions, which are coordinated to only two calcium ions, has expanded somewhat to 2.39 Å, but the other Ca–F bond has contracted substantially to 2.23 Å. The fluoride ion diagonally below the surface fluoride, also has two contracted bond lengths to the calciums below and in the plane (2.33 and 2.36 Å) but the calcium ion above it has relaxed away from it towards the surface, with a resulting Ca–F bond length of 2.53 Å. Thus, in the surfaces where the fluoride channels are either perpendicular or parallel to the surface, we see either distortion of the F–F bond distances or of the Ca–F bond lengths. However, in the {10$\bar{1}$1} surface, which has the fluoride channels lying at an angle with respect to the surface, we find that on geometry optimisation both F–F and Ca–F distortion occurs in the surface region.

The {11$\bar{2}$0}, {10$\bar{1}$3} and {11$\bar{2}$1} surfaces all show similar rearrangements of the surface regions as the {0001}, {10$\bar{1}$0} and {10$\bar{1}$1} surfaces described above, with relaxation of surface calcium ions into the bulk, rotation of the surface phosphate groups and distortion of the chains of fluoride ions.

Hydrated surfaces

We next hydrated the surfaces in a series of partial coverages up to full monolayer coverage, which is here defined as the maximum number of water molecules that could be accommodated on the surface before formation of a second water layer occurred. In a previous molecular dynamics study of water adsorption at MgO surfaces, it was shown that there is a clear difference between the monolayer of water adsorbed at the mineral surface and the bulk water, the liquid structure of which was disturbed by the adsorbed water molecules, leading to a gap of low water density in between the two types of water.[26] Only the adsorbed water monolayer was shown to affect the structure and energy of the underlying surface and in this study we therefore only consider an adsorbed monolayer. The surface and hydration energies of the hydrated surfaces are collected in Table 5, from which we see that hydration has a stabilising effect on all the surfaces considered. However, the {0001} surface is still the dominant plane, followed by the {10$\bar{1}$1} surface.

Fig. 5. shows a bird's eye view of the {0001} surface with a

Table 5 Surface and hydration energies of hydrated fluorapatite surfaces

Surface	γ_{hyd}/J m^{-2}	E_{hyd}/kJ mol^{-1}	Coverage (H_2O/nm^2)
(0001)	0.45	−73	6.6
(10$\bar{1}$0)	0.75	−87	7.8
(10$\bar{1}$1)	0.61	−83	6.0
(11$\bar{2}$0)	0.72	−88	5.4
(10$\bar{1}$3)	1.67	−78	4.6
(11$\bar{2}$1)	0.88	−81	3.7

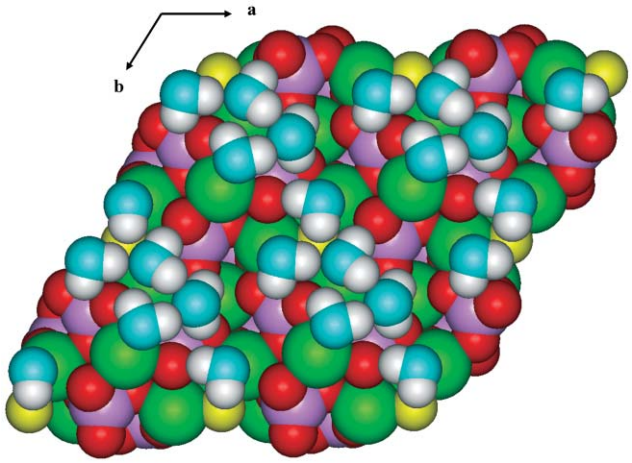

Fig. 5 Plan view of the hydrated {0001} surface, showing an irregular adsorption pattern with clustering of the water molecules round the surface calcium ions (Ca = green, O = red, O_w = pale blue, P = purple, F = yellow, H = white).

full monolayer of adsorbed water. The water molecules do not adsorb in a regular pattern, which is sometimes the case for mineral surfaces, for example the dominant calcite {10$\bar{1}$4} and fluorite {111} surfaces.[41] However, the apatite {0001} with its surface calcium vacancies is itself a much less regular surface than the calcite and fluorite planes, and instead of a regular pattern of adsorption, the water molecules cluster around the remaining surface calcium ions and to a lesser extent exposed calcium ions in the second layer. The major interaction of the water molecules is by their oxygen ions with these surface calcium ions at bond distances of between 2.39 and 2.62 Å, while secondary interactions include hydrogen bonding to surface oxygen (1.86–2.25 Å) and fluoride ions (2.34–2.94 Å). Additional stabilisation of the water layer is provided by a network of intermolecular hydrogen bonding between the water molecules themselves (2.09–2.74 Å). The presence of water has lessened the relaxation of the surface ions somewhat through the provision of extra bonding by the surface ions to water molecules. For example, the surface calcium ions have not receded into the bulk material as much and the fluoride channel is distorted to a lesser extent (between 3.24 and 3.81 Å instead of between 3.20 and 3.86 Å, a fluctuation of 16% instead of 19%).

Fig. 6. shows a side view of the {10$\bar{1}$0} surface with an adsorbed monolayer of water molecules. Again the water molecules cluster round the surface calcium ions but do not form a regular adsorption pattern. Like the dry {10$\bar{1}$0} surface, the F–F distance in the channel remains at its bulk value of 3.43 Å, but the Ca–F bonds are still distorted from their bulk value of 2.37 Å to the values shown in Fig. 6. Thus, like the {0001} surface above, hydration of the {10$\bar{1}$0} does not lead to undistorted fluoride channels, although the distortion of the channels in the surface region is less than for the unhydrated {10$\bar{1}$0} plane, both for the expansion and contraction of Ca–F bonds. A similar situation is seen upon hydration of the {10$\bar{1}$1} surface. The F–F distances are no longer contracted or expanded from their bulk value, but the Ca–F bonds are still distorted to a certain extent, similar to the hydrated {10$\bar{1}$0} surface. Adsorption of water at the {11$\bar{2}$0}, {10$\bar{1}$3} and {11$\bar{2}$1} surfaces shows similar behaviour to the three surfaces described

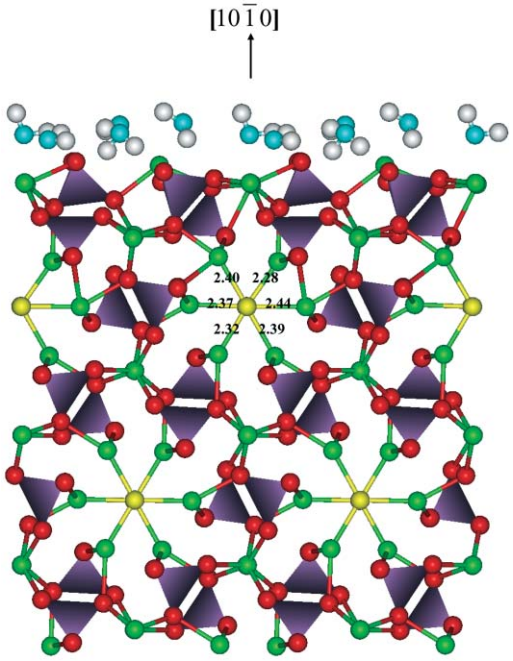

Fig. 6 Side view of the hydrated {10$\bar{1}$0} surface, showing a decreased distortion of the hexagonal channels (Ca = green, O = red, O_w = pale blue, P = purple, F = yellow, H = white, PO_4 groups displayed as tetrahedra).

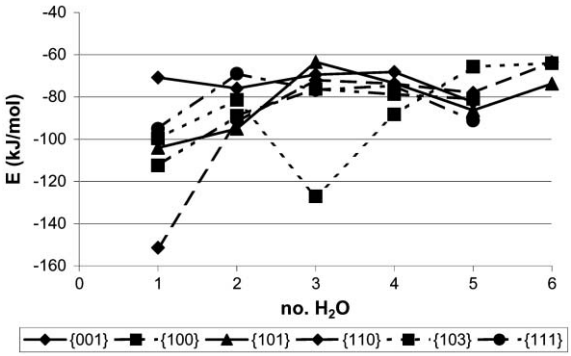

Fig. 7 Sequential energies of adsorption of successive water molecules at the apatite surfaces.

above, with the water molecules mainly coordinating by their oxygen atoms to the surface calcium vacancies but also forming hydrogen-bonded interactions to surface oxygen and fluoride ions and, where possible, to other water molecules. In all cases, the effect of the adsorbed water is to lessen surface relaxation and bond distortion.

The average hydration energies for the adsorption of full monolayers of water on the surfaces are listed in Table 5. They do not vary much from surface to surface, due to the very similar adsorption behaviour at the different surfaces, and the range from -73 kJ mol^{-1} at the {0001} surface to -88 kJ mol^{-1} at the {10$\bar{1}$1} surface indicates physisorption of the (molecular) water at all surfaces. In addition, rather than the average hydration energies for the adsorption of a full layer of water, in Fig. 7 we show a graph of the sequential hydration energies for the different surfaces, where the energy plotted *versus* number of water molecules is the energy released at each addition of a successive water molecule at the surface in question. When adsorbing water at the surfaces, a whole range of starting configurations and adsorption sites for the water molecules were calculated and the values shown are those releasing the most energy at each step, thus ensuring that the most reactive site available was chosen for each successive addition. It is clear from the graph in Fig. 7 that most surfaces exhibit more or less Langmuir behaviour, especially after the initial adsorption of the first water molecule, with the notable exception of the {10$\bar{1}$3} surface, which shows more variation in its hydration energies with the addition of successive water molecules. The {10$\bar{1}$3} surface is a less tightly packed surface than the others with a large surface area of 2.4 nm^2 per unit cell (*cf.* 0.8 nm^2 for the {0001} surface), leading to many different adsorption sites than on the closely packed surfaces. The {11$\bar{2}$1} also has a fairly large surface area per unit cell (1.1 nm^2) and this surface also shows a less regular adsorption behaviour than the other planes.

Morphologies

The equilibrium morphology of a crystal is determined by the surface energy and the related growth rate of the various surfaces and provides a measure of the relative stabilities of the surfaces. Wulff's Theorem[42] showed that a polar plot of surface energy *versus* orientation of normal vectors would give the crystal morphology based on the approach of Gibbs,[43] who proposed that under thermodynamic control the equilibrium form of a crystal should possess minimal total surface free energy for a given volume. Moreover, a surface with a high surface free energy is expected to have a large growth rate and this fast growing surface will not be expressed in the morphology of the resulting crystal. Only surfaces with low surface free energies and hence slow growing will be expressed. Molecular and lattice dynamics simulations have shown that

the contribution of the excess entropy term to the surface free energy in ionic solids is small compared to the enthalpy term, as the differences between the entropies of the bulk and the surface are small.[44,45] In addition, although Mulheran[46] showed that the change in surface free energy with temperature may be significant, Allan and coworkers[45,47] calculated that this change is similar for different surfaces. Hence, for ionic solid surfaces the surface energies are good approximations for the surface free energies, especially taking into account that in morphology calculations only the relative values of the surface free energies of the different faces are important. Thus, the surface energies can be assumed to determine the equilibrium morphology of the crystal and indeed the prediction of morphologies of even complex oxides on the basis of static surface energies has been shown in the past to successfully reproduce experimental morphologies.[48,49] Although in metals and more covalent solids the contribution of entropy to the surface free energy may be more important, *e.g.* ref. 50, recent electronic strucure calculations have shown that fluorapatite is a highly ionic solid, where the PO_4 groups act as polyanions,[31,40] in a similar way to other solids containing molecular anions, such as carbonates and sulfates. For both these systems, accurate morphologies have been predicted on the basis of the static surface energies, which were found to agree with experimentally observed morphologies.[34,51,52]

Fig. 8 shows the calculated morphologies of the fluorapatite crystal, indicating the surfaces expressed in the morphologies. Fig. 8(a) and (b) show the morphologies calculated respectively from the unrelaxed and relaxed surface energies in Table 4, where the dominant {0001} surface is expressed in both cases. When surface relaxation is taken into account, the $\{11\bar{2}1\}$ surface has become relatively more stable than the $\{10\bar{1}1\}$ and $\{11\bar{2}0\}$ surfaces and hence appears in the relaxed crystal morphology (Fig. 8b), in agreement with experimental crystal growth where the $\{11\bar{2}1\}$ surface is found to be a twinning plane for the intergrowth of apatite crystals.[1] When the surfaces are hydrated, the morphology (Fig. 9) changes again due to the dissimilar stabilisation of the different surfaces by the adsorption of water. The $\{11\bar{2}1\}$ surface has disappeared again, but now the $\{10\bar{1}0\}$ surface has become relatively more stable and is hence expressed in the hydrated morphology. The presence of both {0001} and $\{10\bar{1}0\}$ surfaces in the hydrated morphology again agrees with experiment, where both these surfaces are found as cleavage planes[1] and as crystal growth features.[53] Fig. 9(b) is a different view of the same hydrated morphology as in Fig. 9(a), looking down upon the {0001} surface. From the combination of both perspectives, we can see that the hydrated crystals have a rounded hexagonal shape and are fairly flat platelets, in agreement with experimental apatite crystals in bone, which are found to be nanosized platelets.[28,54]

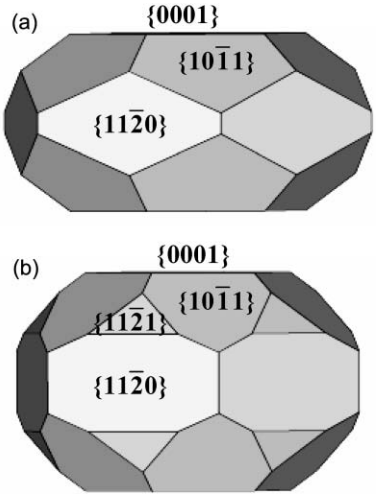

Fig. 8 Calculated thermodynamical morphologies of (a) the unrelaxed and (b) the fully relaxed apatite crystals.

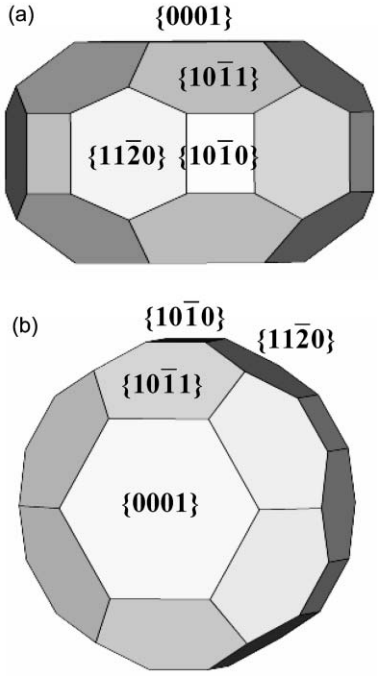

Fig. 9 (a) Side and (b) plan view of the calculated thermodynamical morphologies of the hydrated apatite crystal.

Conclusions

We have employed computational techniques to investigate the effect of water on the surface structure and morphology of the complex fluorapatite material. The potential parameter set derived for fluorapatite is fully compatible with established potential models for both calcite and fluorite minerals and water. The structure, elastic constants and mean vibrational frequencies of the phosphate groups, to which the potential model was fitted, are reproduced accurately, while the calculated static relative permittivities are also in adequate agreement with experiment, even though these were not used in the fitting process.

The {0001} surface is by far the most stable surface, both under dehydrated and hydrated conditions, and is expressed in all three morphologies: bulk-terminated, dry and hydrated crystals. The {0001} surface's dominance is in agreement with its rôle as the major experimental cleavage plane. When surface relaxation of the crystal is taken into account, the morphology of the dry crystal also expresses the major experimental $\{11\bar{2}1\}$ twinning plane, while the hydrated crystal morphology also shows the other $\{10\bar{1}1\}$ cleavage plane in addition to the {0001} surface.

Hydration of the surfaces shows Langmuir behaviour, apart from the rather unstable and open-structured $\{10\bar{1}3\}$ surface, where the energies of sequential hydration show more variation. The calculated hydration energies clearly indicate associative physisorption of the water molecules. The adsorption of water and hence increased coordination of the surface ions has a stabilising effect on all surfaces, particularly the four closest-packed planes, the {0001}, $\{10\bar{1}0\}$, $\{10\bar{1}1\}$ and $\{11\bar{2}0\}$ surfaces, whose surface energies all decrease by 35–43% upon hydration. The overall effect of the water monolayer is to lessen the relaxation of the surface regions compared to the dehydrated surface, leading to more bulk-like terminations. The surface energies of the two twinning planes, the $\{10\bar{1}3\}$ and

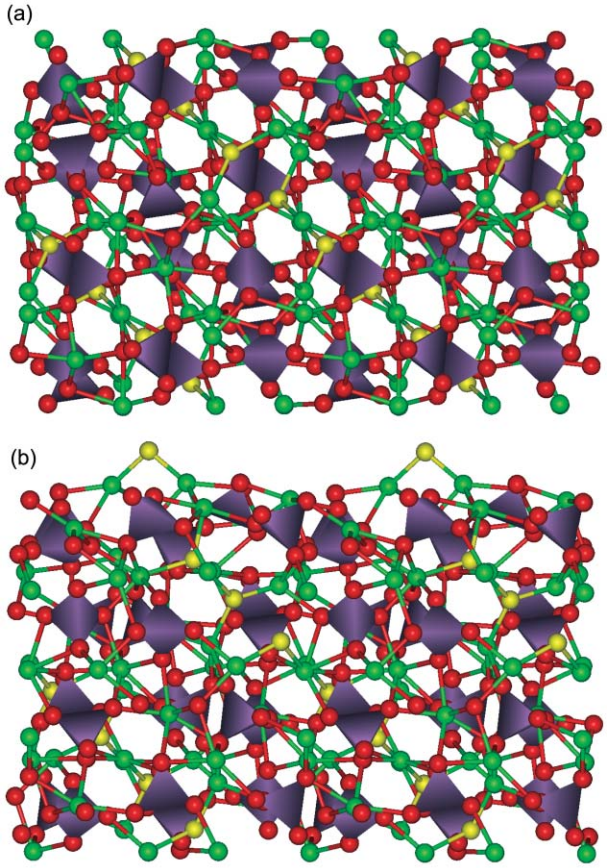

Fig. 10 Side view of (a) the bulk-terminated and (b) the fully geometry optimised structure of the $\{11\bar{2}1\}$ surface, showing extensive surface relaxations and phosphate rotations throughout a surface region of approximately ~15 Å (Ca = green, O = red, P = purple, F = yellow, PO_4 groups displayed as tetrahedra).

$\{11\bar{2}1\}$ surfaces, which have a much less close-packed structure are less severely affected by water adsorption, only decreasing by 14–21% from their value in the dry crystal. Although these surfaces are less closely packed than the other four, their interlayer spacings are smaller and hence the ions in the surface region, although not as well coordinated laterally to other surface ions, are more closely coordinated to ions below the surface. The major stabilisation of these two surfaces is therefore due to extensive relaxations and rotations of the dry surfaces, decreasing their surface energies by 35–57% with respect to the bulk-terminated surfaces, rather than coordination to water molecules. Fig. 10, for example, shows how upon geometry optimisation of the $\{11\bar{2}1\}$ surface, significant rotation of the phosphate groups occurs, even four layers into the surface (~15 Å), while the surface fluoride ions move out of the surface, forming extra bonds to surface calcium ions which move into the bulk material.

The type of distortion of the fluoride chains in the calcium channels depends upon the orientation of the channels with respect to the surface. When the channels are perpendicular to the surface, only F–F distortion occurs within the channels, whereas when the channels lie in the plane of the surface, the F–F distances are unchanged but the Ca–F bonds are distorted, as was also seen in Lee *et al.*'s study of slabs of apatite material,[28] and the F–F chains form a zig-zag pattern through the channel. A mixture of both distortions occurs when the channels lie at an angle to the surface.

Future work will include calculations of impurity uptake into the apatite crystal, such as Mg ions and CO_3 groups, which are important substitutional defects in bone material, and the investigation of calcite/apatite and fluorite/apatite interfaces.

Acknowledgements

We thank Drs J. D. Gale and S. M. Woodley and Professors C. R. A. Catlow and P. E. Ngoepe for useful discussions. DM acknowledges the Royal Society and the NRF and CSIR, South Africa for financial support. NHdL acknowledges NERC grant no. NER/M/S/2001/00068, EPSRC grant no. GR/N65172/01, the Royal Society, grant no. 22292, and the Wellcome Trust, grant no. 065067, for financial support. We wish to acknowledge the use of the EPSRC's Chemical Database Service at Daresbury.

References

1 W. A. Deer, R. A. Howie and J. Zussman, in *An introduction to the rock-forming minerals*, Longman, UK, 1992.
2 J. C. Elliott, in *Structure and chemistry of the apatites and other calcium orthophosphates, Studies in inorganic chemistry 18*, Elsevier, Amsterdam, 1994.
3 R. L. Romer, *Geochim. Cosmochim. Acta*, 1996, **60**, 1951.
4 M. Menzies, K. Gallagher, A. Yelland and A. J. Hurford, *Geochim. Cosmochim. Acta*, 1997, **61**, 2511.
5 F. Corfu and D. Stone, *Geochim. Cosmochim. Acta*, 1998, **62**, 2979.
6 P. Pellas, C. Fieni, M. Trieloff and E. K. Jessberger, *Geochim. Cosmochim. Acta*, 1997, **61**, 3477.
7 R. A. Wolf, K. A. Farley and L. T. Silver, *Geochim. Cosmochim. Acta*, 1996, **60**, 4231.
8 K. A. Farley, R. A. Wolf and L. T. Silver, *Geochim. Cosmochim. Acta*, 1996, **60**, 4223.
9 T. Sasada, H. Hiyagon, K. Bell and M. Ebihara, *Geochim. Cosmochim. Acta*, 1997, **61**, 4219.
10 A. C. Warnock, P. K. Zeitler, R. A. Wolf and S. C. Bergman, *Geochim. Cosmochim. Acta*, 1997, **61**, 5371.
11 T. J. McCoy, M. Wadhwa and K. Keil, *Geochim. Cosmochim. Acta*, 1999, **63**, 1249.
12 S. K. Lower, P. A. Maurice and S. J. Traina, *Geochim. Cosmochim. Acta*, 1998, **62**, 1773.
13 M. Born and K. Huang, *Dynamical Theory of Crystal Lattices*, Oxford University Press; Oxford, 1954.
14 B. G. Dick and A. W. Overhauser, *Phys. Rev.*, 1958, **112**, 90.
15 A. Pavese, M. Catti, S. C. Parker and A. Wall, *Phys. Chem. Miner.*, 1996, **23**, 89.
16 N. H. de Leeuw and S. C. Parker, *J. Chem. Soc., Faraday Trans.*, 1997, **93**, 467.
17 N. H. de Leeuw, S. C. Parker and J. H. Harding, *Phys. Rev. B*, 1999, **60**, 13792.
18 N. H. de Leeuw and S. C. Parker, *J. Chem. Phys.*, 2000, **112**, 4326.
19 N. H. de Leeuw and S. C. Parker, *Phys. Chem. Chem. Phys.*, 2001, **3**, 3217.
20 S. C. Parker and G. D. Price, *Adv. Solid State Chem.*, 1989, **1**, 295.
21 J. D. Gale, *J. Chem. Soc., Faraday Trans.*, 1997, **93**, 629.
22 G. W. Watson, E. T. Kelsey, N. H. de Leeuw, D. J. Harris and S. C. Parker, *J. Chem. Soc., Faraday Trans.*, 1996, **92**, 433.
23 P. W. Tasker, *Philos. Mag. A*, 1979, **39**, 119.
24 D. E. Parry, *Surf. Sci.*, 1975, **49**, 433.
25 D. E. Parry, *Surf. Sci.*, 1976, **54**, 195.
26 N. H. de Leeuw and S. C. Parker, *Phys. Rev. B*, 1998, **58**, 13901.
27 Z. Duan, N. Moller and J. H. Weare, *Geochim. Cosmochim. Acta*, 1995, **59**, 3273.
28 W. T. Lee, M. T. Dove and E. K. H. Salje, *J. Phys. Condens. Matter*, 2000, **12**, 9829.
29 C. Meis, J. D. Gale, L. Boyer, J. Carpena and D. Gosset, *J. Phys. Chem. A*, 2000, **104**, 5380.
30 C. R. A. Catlow, M. J. Norgett and A. Ross, *J. Phys. C*, 1977, **10**, 1630.
31 N. H. de Leeuw, *Chem. Mater.*, 2002, **14**, 435.
32 D. R. Lide, in *CRC Handbook of Chemistry and Physics*, CRC, Boca Raton, FL, 2000.
33 M. G. Taylor, S. F. Parker, K. Simkiss and P. C. H. Mitchell, *Phys. Chem. Chem. Phys.*, 2001, **3**, 1514.
34 N. H. de Leeuw and S. C. Parker, *J. Phys. Chem. B*, 1998, **102**, 2914.
35 N. H. de Leeuw and S. C. Parker, *Mol. Simul.*, 2000, **24**, 71.
36 S. B. Hendricks, M. E. Jefferson and V. M. Mosley, *Z. Kristall. Kristallgeom. Kristallphys. Kristallchem.*, 1932, **81**, 352.
37 R. D. Shannon and G. R. Rossman, *Phys. Chem. Miner.*, 1992, **19**, 157.
38 www.milltronics-tx.com.

39 S. Hontsu, T. Matsumoto, J. Ishii, M. Nakamori, H. Tabata and T. Kawai, *Thin Solid Films*, 1997, **295**, 214.
40 N. H. de Leeuw, *Chem. Commun.*, 2001, 1646.
41 N. H. de Leeuw, S. C. Parker and K. Hanumantha Rao, *Langmuir*, 1998, **14**, 5900.
42 G. Wulff, *Z. Kristallogr. Kristallgeom.*, 1901, **39**, 449.
43 J. W. Gibbs, in *Collected works*, Longman, New York, 1928.
44 S. C. Parker, 2002, personal communication.
45 M. B. Taylor, C. E. Sims, G. D. Barrera and N. L. Allan, *Phys. Rev. B*, 1999, **59**, 6742.
46 P. A. Mulheran, *Philos. Mag. A*, 1993, **68**, 799.
47 N. L. Allan, G. D. Barrera, J. A. Purton, C. E. Sims and M. B. Taylor, *Phys. Chem. Chem. Phys.*, 2000, **2**, 1099.
48 S. C. Parker, E. T. Kelsey, P. M. Oliver and J. O. Titiloye, *Faraday Discuss.*, 1993, **95**, 75.
49 N. H. de Leeuw, S. C. Parker, C. R. A. Catlow and G. D. Price, *Phys. Chem. Miner.*, 2000, **27**, 332.
50 N. M. Harrison, X.-G. Wang, J. Muscat and M. Scheffler, *Faraday Discuss.*, 1999, **114**, 305.
51 J. O. Titiloye, S. C. Parker and S. Mann, *J. Cryst. Growth*, 1993, **131**, 533.
52 D. H. Gay and A. L. Rohl, *J. Chem. Soc., Faraday Trans.*, 1995, **91**, 925.
53 J. Rakovan and R. J. Reeder, *Am. Miner.*, 1994, **79**, 892.
54 S. Weiner and H. D. Wagner, *Ann. Rev. Mater. Sci.*, 1998, **28**, 271.
55 M. C. Sha, Z. Li and R. C. Brandt, *J. Appl. Phys.*, 1994, **75**, 7784.
56 P. Comodi, Y. Liu, P. F. Zanazzi and M. Montagnoli, *Phys. Chem. Miner.*, 2001, **28**, 219.